PAPER

Time-resolved signatures across the intramolecular response in substituted cyanine dyes†

Muath Nairat, [ID] [a] Morgan Webb,[a] Michael P. Esch,[a] Vadim V. Lozovoy,[a] Benjamin G. Levine[a] and Marcos Dantus*[ab]

The optically populated excited state wave packet propagates along multidimensional intramolecular coordinates soon after photoexcitation. This action occurs alongside an intermolecular response from the surrounding solvent. Disentangling the multidimensional convoluted signal enables the possibility to separate and understand the initial intramolecular relaxation pathways over the excited state potential energy surface. Here we track the initial excited state dynamics by measuring the fluorescence yield from the first excited state as a function of time delay between two color femtosecond pulses for several cyanine dyes having different substituents. We find that when the high frequency pulse precedes the low frequency one and for timescales up to 200 fs, the excited state population can be depleted through stimulated emission with efficiency that is dependent on the molecular electronic structure. A similar observation at even shorter times was made by scanning the chirp (frequencies ordering) of a femtosecond pulse. The changes in depletion reflect the rate at which the nuclear coordinates of the excited state leave the Franck–Condon (FC) region and progress towards achieving equilibrium. Through functional group substitution, we explore these dynamic changes as a function of dipolar change following photoexcitation. Density functional theory calculations were performed to provide greater insight into the experimental spectroscopic observations. Complete active space (CAS) self-consistent field and CAS second order perturbation theory calculated potential energy surfaces tracking twisting and pyramidalization confirm that the steeper potential at the FC region leads to the observation of faster wave packet dynamics.

Introduction

The molecular dynamics following photoexcitation are determined during the first tens of femtoseconds. Upon formation, the excited state wave packet is no longer considered in equilibrium with either the nuclear degrees of freedom or the surrounding solvent. The excited state potential determines the ensuing dynamics towards equilibrium. Achieving equilibrium requires involvement from both intra- and inter-molecular modes through multidimensional coordinates which can occur within tens of femtoseconds as in barrierless electron transfer, or takes up to nanoseconds where diffusional solvent transport is crucial for this equilibrium.[1–4] In general, dynamics that take longer than 100 fs are well understood and assigned whereas the early dynamic steps, soon after the absorption of a photon and up to 100 fs, are highly obscured by multiple convoluted signals,[5–8] with an interplay between intra- and inter-molecular

interactions and their corresponding energy fluctuations. So far, ultrafast multidimensional spectroscopic techniques and four-wave mixing methods have been successfully implemented to achieve an understanding of the early timescale processes.[9,10] However, their implementation requires precise control over a sequence of multiple pulses and a rigorous theoretical treatment to understand the detected signals and how they relate to molecular dynamics.[11] In our current work, we show that single beam pulses with a well-defined phase can be used to extract early dynamic information that is not easily obtained by other methods. Single shaped-pulse approaches have the additional advantage that they may be used on single nanoparticles or molecules.[12]

Cyanines are a class of polymethine dyes that consist of an odd number of conjugated $2p_z$ orbitals. Their structure resembles carotenoids and protonated Schiff bases, making them an ideal system to model and understand the excited state dynamics of conjugated polyene systems in general. Moreover, cyanines have applications in photodynamic therapy,[13] solar energy conversion,[14] and bioimaging.[15] Generally, they are positively charged compounds with an alternating and delocalized electron density between the polymethine two ends.[16–18] Cyanines have an optically active S_0–S_1 transition in the visible or near-infrared region that is highly dependent on the backbone length.[19]

[a] *Department of Chemistry, Michigan State University, East Lansing, Michigan 48824, USA. E-mail: dantus@msu.edu*

[b] *Department of Physics and Astronomy, Michigan State University, East Lansing, Michigan 48824, USA*

This journal is © the Owner Societies 2017

Phys. Chem. Chem. Phys., 2017, **19**, 14085–14095 | 14085

The ground state electronic structure of cyanine dyes can be viewed as a combination of three configurations: two degenerate resonance structures wherein the positive charge is localized at either end of the conjugated chain and a charge centered configuration.[20] These three resonance structures are considered to contribute equally to the wave function, hence the charge remains delocalized and the polymethine structure exhibits minimal carbon-carbon bond length alteration (BLA).[21] The S_0–S_1, $\pi \rightarrow \pi^*$, optical transition occurs without a significant change in the permanent dipole moment and hence can be described by invoking a nonpolar solvation response.[17,22] Upon the addition of an electron donating group to the central carbon of the backbone, cyanine dyes exhibit an electronic configuration where the positive charge predominantly remains at this central position to form what is termed as a bis-dipolar configuration.[23] In addition, this configuration exhibits an additional symmetric ground state resonance structure that does not contribute to the asymmetric excited state structure.[24] Therefore, optical excitation of substituted cyanines is accompanied by a significant change in the dipole moment that triggers a polar solvation response,[24,25] causing the reorientation of solvent molecules. The progress of the molecular relaxation soon after photoexcitation proceeds simultaneously through intra- and inter-molecular modes as illustrated in the schematic representation in Fig. 1.

Our group has been taking advantage of the ability to manipulate the arrival times of the spectral components in a broadband femtosecond pulse to control nonlinear optical processes and develop novel spectroscopic methods.[26,27] By controlling chirp, the molecular dynamics can be probed directly using a single shaped pulse;[25,28–30] this approach can serve to study ultrafast processes soon after photoexcitation; as demonstrated in this work for a set of cyanine dyes with rational variations in their structure and their optical properties. Pulse shaping in general has been implemented in multidimensional spectroscopy to provide versatility in tailoring and controlling the pulses at the sample position.[31–33] It also provides the ability to suppress undesired signal pathways.[34]
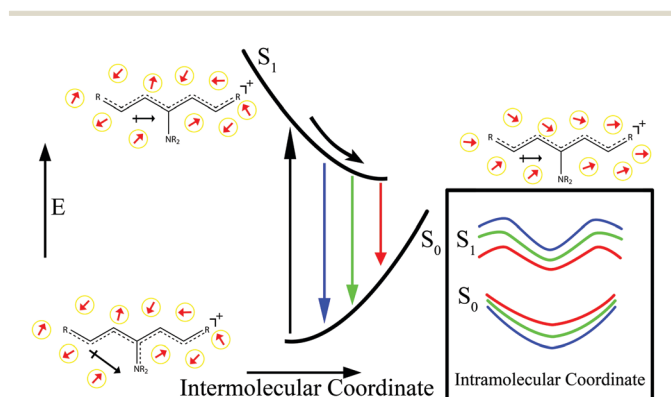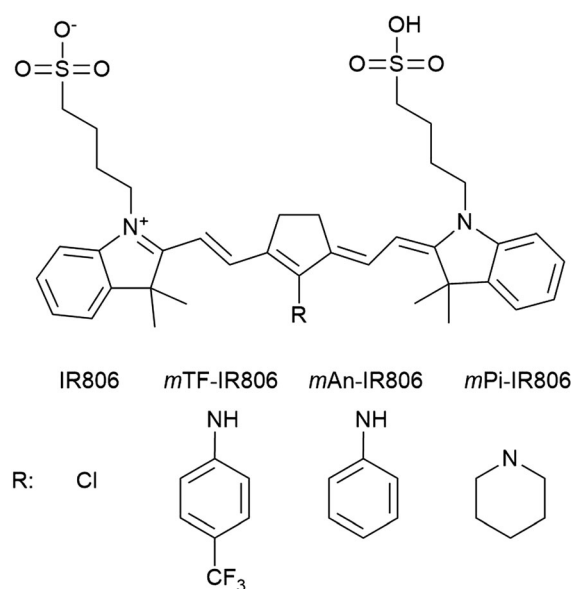
Experimental

Synthesis

The experiments were carried out using the cyanine dyes shown in Scheme 1. IR806 (Sigma-Aldrich) was used as purchased without further purification. The other cyanine dyes were synthesized according to a published procedure[35] starting from IR806 with rational variation of the substituent at the cyanine meso-position, that is the central carbon across the polymethine chain.

meso-Trifluoromethylaniline IR806 (*m*TF-IR806): IR806 (0.1 mmol, 1 eq.) was stirred in DMF at 80 °C. Then 4-(trifluoromethyl)aniline (1 mmol, 10 eq.) was added and the mixture was kept under stirring for 8 h. After DMF evaporation the crude mixture was purified using chromatography on silica gel with DCM/MeOH (99 : 1–95 : 5). Dark blue solid was obtained with a ~20% yield. δ_H (500 MHz, methanol-d_4) 7.77 (2H, d, J 13.3), 7.72 (2H, d, J 8.3), 7.48 (2H, d, J 8.3), 7.31 (4H, t, J 7.5), 7.18 (2H, d, J 7.9), 7.11 (2H, t, J 7.4), 5.85 (2H, d, J 13.4), 4.61 (1H, s), 4.04 (4H, t, J 6.9), 2.90 (4H, s), 2.86 (4H, t, J 7.0), 1.98–1.86 (8H, m), 1.39 (12H, s).

meso-Aniline IR806 (*m*An-IR806): IR806 (0.02 mmol, 1 eq.) was stirred in DMF at room temperature. Then aniline (0.1 mmol, 5 eq.) was added and the mixture was kept under stirring for 12 h. Dark blue solid was obtained with a ~90% yield. δ_H (500 MHz, methanol-d_4) 7.77 (2H, d, J 13.0), 7.52 (2H, t, J 7.8), 7.48–7.40 (4H, m), 7.35–7.21 (4H, m), 7.11 (2H, d, J 8.1), 7.07 (2H, t, J 7.5), 5.73 (2H, d, J 13.1), 3.98 (4H, t, J 6.6), 2.86 (8H, d, J 5.8), 1.96–1.85 (8H, m), 1.37 (12H, s).

meso-Piperidine IR806 (*m*Pi-IR806): IR806 (0.02 mmol, 1 eq.) was stirred in DMF at room temperature. Then piperidine (0.1 mmol, 5 eq.) was added and the mixture was kept under stirring for 16 h. After DMF evaporation, dark blue solid was obtained with a ~90% yield. δ_H (500 MHz, DMSO-d_6) 7.67 (2H, d, J 13.1), 7.48 (2H, d, J 7.4), 7.32 (2H, t, J 7.7), 7.23 (2H, d, J 7.9),

Fig. 1 Schematic representation for the intermolecular solvation potentials of a cyanine dye where the surrounding solvent responds to the change in the cyanine dipole moment associated with photoexcitation. Relaxation across the intermolecular coordinate is coupled with changes in the multidimensional intramolecular coordinate.

Scheme 1 Chemical structures for the cyanine dyes considered in this work.

7.10 (2H, t, *J* 7.5), 5.77 (2H, d, *J* 13.2), 3.99 (4H, t, *J* 7.8), 3.01 (4H, t, *J* 5.6), 2.47 (4H, t, *J* 7.2), 1.79–1.73 (4H, m), 1.74–1.66 (4H, m), 1.67–1.60 (4H, m), 1.60 (12H, s), 1.58–1.53 (2H, m).

Steady state spectroscopy

UV-visible absorbance spectra were recorded using an ATI/ Unicam UV2 model for IR806 while dissolved in methanol (MeOH) and the remaining substituted cyanine dyes while dissolved in *n*-propanol (PrOH). PrOH has been used with the substituted dyes to have absorption spectra that are red shifted compared to MeOH, providing better overlap with the excitation laser in the later experiments. Fluorescence spectra for all the dyes while dissolved in the aforementioned solvents were obtained using a Hitachi FL-4500 fluorescence spectrometer.

Laser experiments

The laser excitation and fluorescence detection experiments were carried out using IR806 dissolved in MeOH, while the remaining dyes were dissolved in PrOH. The starting concentration was 50 μM and further dilutions were made, if necessary, to achieve an optical density value of 0.3 with the excitation laser. The experimental setup consists of a regeneratively amplified Ti:sapphire laser (Spitfire, Spectra-Physics, Santa Clara, CA) producing femtosecond pulses at a repetition rate of 1 kHz. The pulses were compressed and shaped after the amplifier with a pulse shaper (MIIPS-HD, Biophotonic Solutions Inc., East Lansing, MI) using the Multiphoton Intrapulse Interference Phase Scan (MIIPS) method.[36,37] The laser pulse-to-pulse stability was ensured with a fidelity value of 0.9.[38] IR806 and *m*TF-IR806 were excited using near-Gaussian pulses centered at 800 nm with 25.9 nm fwhm bandwidth. The pulse bandwidth corresponds to a pulse duration of 37 fs (when transform-limited, TL). While *m*An-IR806 and *m*Pi-IR806 were excited using near-Gaussian pulses centered at 790 nm with a pulse duration of 35 fs (when TL). In all experiments, unfocused 25 μJ pulses were sent onto a cuvette having a 2 mm path length. Fluorescence signal was detected at a right angle from the excitation axis near the entrance of the cuvette window using a multimode optical fiber connected with a compact spectrometer (USB4000, Ocean Optics). The stimulated emission signal was detected along the laser propagation axis after the cuvette.

The pulses were compressed to TL at the sample location and were further shaped while detecting the fluorescence signal simultaneously. Using the pulse shaper, chirp scan was carried out by applying a chirp phase mask of the form $\phi(\omega) = 0.5\phi''(\omega - \omega_0)^2$, where ϕ'' is the quadratic phase or the chirp value. The chirp value was scanned from negative to positive 20 000 fs². Chirp on the TL pulse stretches it to longer durations according to $\tau/\tau_{TL} = \sqrt{1 + (4\ln 2)^2(\phi''/\tau_{TL}^2)^2}$. In the case of negative chirp, the high frequency components precede the lower ones, whereas the arrival order is reversed with the positive chirp.

Time delay scans were carried out using the pulse shaper by advancing or delaying the frequencies higher than the laser central frequency. The scan displays the fluorescence signal as a function of time delay between the pump and probe pulses.

Computational methods

To investigate the structural changes that accompany the substitution of IR806, ground state geometry optimization for all the cyanine dyes was carried out by density functional theory (DFT) using the 6-311+G(3d,p) basis set. A modified hybrid generalized gradient approximation (GGA) functional of Perdew, Burke and Ernzerhof (PBEα) was used.[39] α, which corresponds to the Hartree–Fock exchange contribution, was tuned to 0.456. The exchange term using this linear combination was found to provide reasonable DFT results in relative agreement with CCSD(T) in terms of the cyanine BLA.[40] Atomic charges were computed for the optimized ground state geometry using the natural bond orbital (NBO) analysis.[41] Excited state energies were calculated by the time-dependent DFT (TDDFT) formalism using the 6-311+G(3d,p) basis set to model the experimentally observed blue shift in the absorption maxima of the cyanines as a function of substituent. When TDDFT was employed, both the ground state geometry optimization and the vertical excitation were carried out using the PBE functional.[42] Using this functional, reasonable vertical excitation energies for the cyanine dyes can be obtained.[43,44] All ground state geometry optimizations were followed by frequency calculations to ensure the absence of imaginary eigenvalues and confirm the minimum structure. Solvent effects were incorporated using the Integral Equation Formalism Polarizable Continuum Model (IEF-PCM),[45] wherein equilibrium solvation was used in the ground state optimization and non-equilibrium solvation with linear response was used in the excited state calculation. MeOH was used with IR806 while PrOH was used with the other dyes.

To understand the role of the substituent on the intramolecular response of cyanines, the minimum energy path (MEP) on the excited state potential energy surfaces of simpler cyanine dyes was modeled at the complete active space self-consistent field (CASSCF) level with 6-31G(d) as a basis set. The ground state geometry was obtained at the same level of theory with no symmetry constraints. The MEP on the first excited state potential was followed from the Franck–Condon (FC) region down to the emissive excited state minima, state averaging both the ground and the excited state with equal weights. The absence of imaginary frequencies was ensured at both the ground state geometry and the excited state minima. Dynamic electron correlation was accounted for at selected nuclear configurations over the CASSCF MEP using multireference second order perturbation theory (CASPT2) with 6-31G(d) as a basis set. CASPT2 was employed without correlating the core electrons on the heavy atoms while also including an IPEA shift of 0.25 Hartree in the evaluation of the zeroth order Hamiltonian.[46] Moreover, the excited state potential energy surfaces for the substituted cyanines were scanned using constrained optimization over the two dihedral angles that represent twisting and pyramidalization of the substituent using CASSCF gradients followed by an evaluation of the energies using CASPT2. The cyanine models were chosen with the same polymethine backbone length, that is 9 carbons between the two terminal nitrogens.

CN11:

CN11N:

CN11NC2:
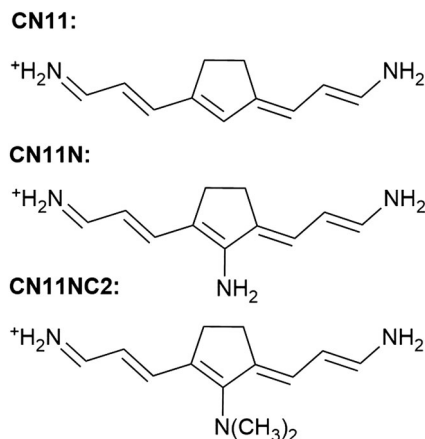
Scheme 2 The chemical structures for the three model cyanine dyes used in the CASSCF calculations.

The central three carbons were also locked using a cyclopentene ring. Three cases were considered: (i) unsubstituted (CN11), (ii) amine substituent (CN11N), (iii) dimethyl amine substituent (CN11NC2). The chemical structures for the three dyes are shown in Scheme 2. For the unsubstituted dye CN11, (12,11) was chosen as the active space, which contains all the conjugated p_z orbitals, whereas (14,12) was considered as an active space for the substituted dyes to include the substituent nitrogen p_z orbital. All DFT and TDDFT calculations were performed using Gaussian 09.[47] CASSCF and CASPT2 calculations were carried out using Molpro 2012.1.[48–52] All structures are provided in the ESI.†

Results

Steady state spectroscopy

The first excited state transition of the cyanine dye IR806, which has minimal BLA and an electronic configuration that is delocalized over the conjugated polymethine backbone, occurs without a significant change in the permanent dipole moment. This $\pi \rightarrow \pi^\star$ transition to the S_1 state results in a sharp absorption spectrum featuring a vibronic shoulder at higher energies as shown in Fig. 2a. The fluorescence spectrum for IR806 exhibits a slight departure from the mirror image symmetry as can be seen in the same figure.

The remaining cyanine dyes share an identical polymethine structure with IR806, yet differ in terms of the *meso*-substituent. Due to this electron donating substituent, they acquire extra contribution from the charge-centered configuration, which permits a polar solvation response. The absorption spectra for all the polar solvated dyes (Fig. 2b–d) are blue shifted with respect to the nonpolar IR806 and are essentially broader, lacking the cyanine vibronic feature observed for IR806. Interestingly, all the polar solvated cyanines show an additional S_2 absorption peak that is emissive.[53,54] The absorption maxima, fluorescence maxima, Stokes shifts and full width at half maxima (fwhm) for the absorption and the fluorescence spectra of all the dyes are given in Table 1.
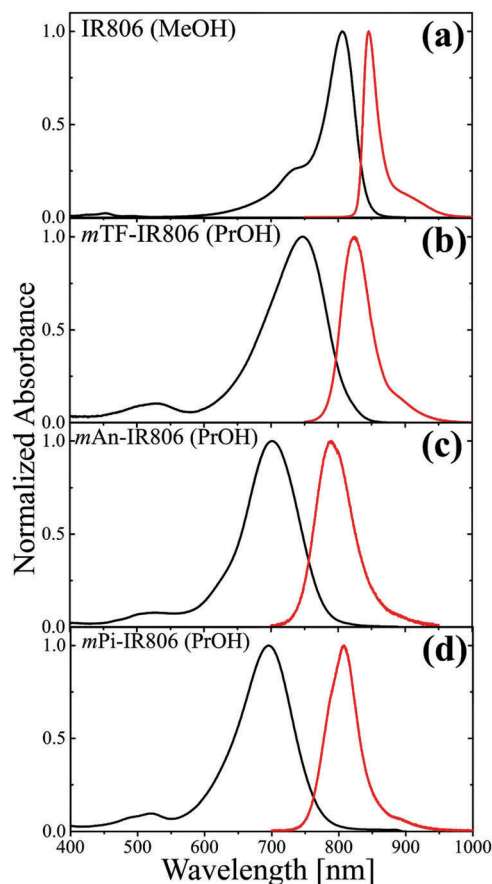

Fig. 2 Steady state absorption (black) and fluorescence (red) spectra for the cyanine dyes (a) IR806, (b) *m*TF-IR806, (c) *m*An-IR806, and (d) *m*Pi-IR806. The used solvent with each dye is indicated in parentheses.
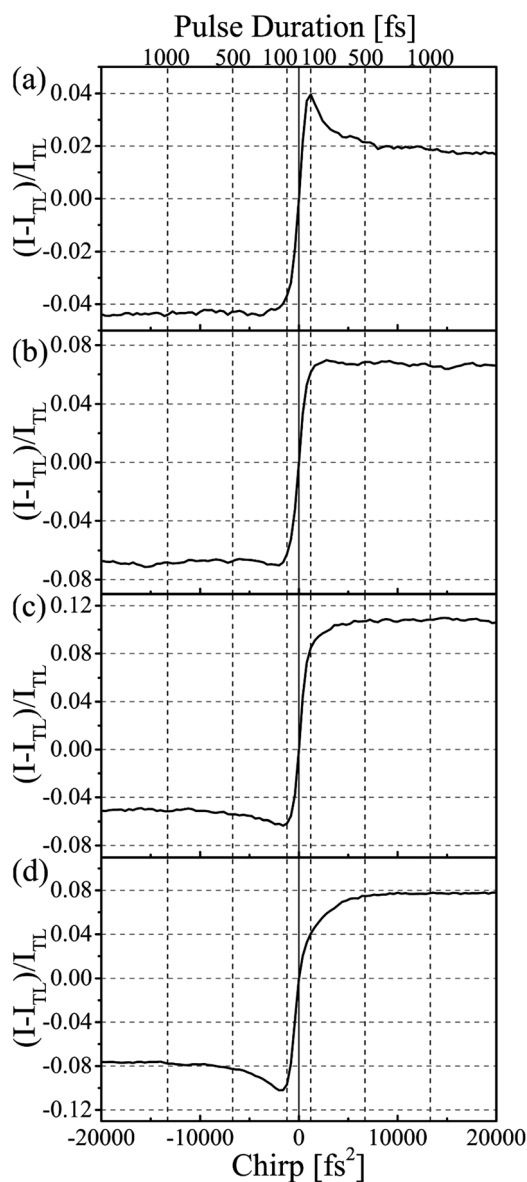
Chirp and time delay measurements

The frequency integrated fluorescence signals from each cyanine dye as a function of linear chirp are shown in Fig. 3. The fluorescence signal is normalized with respect to the signal obtained using TL pulses. The stretched pulse duration is shown on the top axis to elucidate the timescales at which changes are observed in the chirp trace. In all cases, the typical first excited state chirp response is obtained:[28,55] a reduced fluorescence yield while using negatively chirped pulses. The high to low frequencies ordering allows the excited state population to be depleted *via* stimulated emission before intramolecular vibrational redistribution and fluorescence occur.[28] The stimulated emission traces which inversely correlate with the fluorescence traces are provided in the ESI.†

Previous studies showed that the maximum fluorescence depletion, which occurs at a small negative chirp value, is unaffected by the solvent and its temperature,[25] whereas the dependence of fluorescence on positive chirp was observed to change as a function of intermolecular changes *via* solvent and temperature. Changes on both sides of the chirp trace were detected as a result of the appearance of new species with different dynamics; in that case it was the formation of a triplet state.[29] Here we see that IR806 chirp response (Fig. 3a) has a

14088 | *Phys. Chem. Chem. Phys.*, 2017, **19**, 14085–14095

This journal is © the Owner Societies 2017

Table 1 Absorption maxima, fluorescence maxima, Stokes shifts and fwhm of the absorption and the emission spectra of the first excited state (S_1) for IR806, mTF-IR806, mAn-IR806, and mPi-IR806. S_1–S_0 Stokes shift was measured as the difference between the absorption and fluorescence spectra maxima

	IR806 (MeOH)	mTF-IR806 (PrOH)	mAn-IR806 (PrOH)	mPi-IR806 (PrOH)
Abs. max (cm^{-1})	12 407 (806 nm)	13 369 (748 nm)	14 265 (701 nm)	14 368 (696 nm)
Fl. max (cm^{-1})	11 825 (845 nm)	12 127 (825 nm)	12 652 (790 nm)	12 377 (807 nm)
S_1–S_0 Stokes shift (cm^{-1})	582	1242	1613	1991
Abs. fwhm (cm^{-1})	778	1908	1857	1935
Fl. fwhm (cm^{-1})	489	740	1018	834

Fig. 3 Total fluorescence signal as a function of linear chirp for (a) IR806, (b) mTF-IR806, (c) mAn-IR806, and (d) mPi-IR806. Top axis shows the duration of the chirped pulse.

then starts to gradually decrease and becomes constant at large positive chirp values ($\sim$10 000 fs^2); this is also consistent with IR125.[25]

The remaining cyanine dyes show a gradual change in the chirp response (Fig. 3b–d) according to the following order: mTF-IR806, mAn-IR806, then mPi-IR806, which is correlated with the electron donation strength of the substituent. On the negative chirp side, a maximum fluorescence depletion point appears at small chirp values. The chirp values correspond to time delays of $\sim$100 fs, such fast timescales primarily reflect intramolecular modes in the molecule. On the positive side of the chirp trace, the sudden increase in the fluorescence signal is absent. Instead, a gradual increase in the fluorescence signal is observed as a function of increasing chirp value. These changes on the positive side reflect variations in the inter-molecular response for the molecules. For instance, mPi-IR806 which has the strongest electron donation substituent and is expected to be associated with the largest change in dipole moment upon excitation, shows the slowest gradual increase in fluorescence to achieve a constant fluorescence signal.

Pump–probe traces with different frequency pulses generated using the pulse shaper are shown in Fig. 4. Fig. 4a shows the response when the high frequency pulse precedes the lower one, which resembles the negative chirp case. Using this arrival order, the excited state population responsible for fluorescence is depleted compared to what is obtained using TL pulses. Fig. 4b shows the reversed frequencies ordering, that is the low frequency pulse is followed by the higher frequency one (similar to positive chirp). The total fluorescence is normalized with respect to the asymptotic yield at time delays longer than 500 fs. Each trace in Fig. 4 resembles one side of the chirp traces in Fig. 3 and shows the same trend across the dyes when compared carefully.

Quantum chemical calculations & discussion

We performed quantum chemical calculations to explore the electronic properties and potential energy surfaces of the molecules studied experimentally, and how these properties depend on the substituent on the central carbon. This section is divided into three parts. First, we describe DFT calculations that provide a connection between the cyanine structures and the observed optical properties. Second, we describe TDDFT results on the vertical excitation energies of the optimized

constant fluorescence depletion on the negative chirp side, a chirp response that resembles the nonpolar cyanine dye IR125.[25] The positive chirp side shows a sudden increase in the fluorescence signal that reaches a maximum value at 1200 fs^2 ($\sim$100 fs),
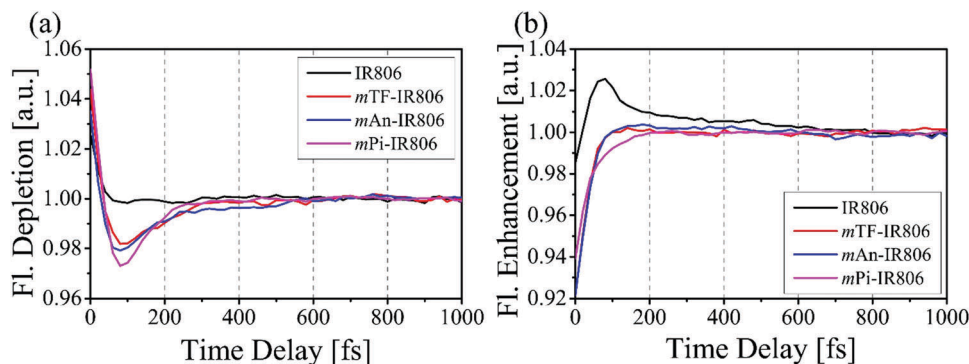
Fig. 4 Total fluorescence signal using two color pump–probe pulses for the four cyanine dyes when (a) the high frequency pulse precedes the lower frequency one and when (b) the arrival order is reversed.

structures, which give us insight into the observed blue shift in the absorption spectra recorded as the substituent electron donation strength increases. Third, we present CASSCF and CASPT2 potential energy surfaces, which provide us with insight into the initial geometry of the excited state wave packet at the FC region, and its evolution towards equilibrium.

The optical properties of cyanine dyes are highly dependent on the BLA,[56] which is the difference between the lengths of single and double bonds along the polymethine backbone. When a cyanine exhibits equal contribution between its two resonance structures, each with the charge localized at either end of the molecule, a net zero BLA is observed. This condition is known as the "cyanine limit". The linear and nonlinear optical properties of cyanines are directly related to the BLA value.[56] At the cyanine limit, the optical transition energy associated with absorption to S_1 is minimized and the spectral transition is sharp.[57] A blue shift (increase in transition energy) along with broadening of the absorption spectrum is expected with increasing BLA for cyanines with the same backbone length. DFT calculations were performed to determine the BLA for the cyanines in this study.

The bond lengths between carbon atoms along the polymethine backbone for the optimized ground state structures were calculated and are shown in Fig. 5. The central carbon is represented with the atomic index 0 while the terminal
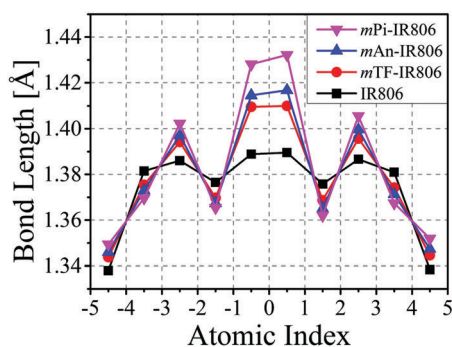
Table 2 The cyanine dyes' TDDFT vertical excitation energies, error relative to the experimental absorption maxima, NBO charge on the central carbon, and the average dihedral angles for the ground state structures

	TDDFT ΔE (cm^{-1})	Err. (cm^{-1})	Charge on central C (e) (PBEα)	Average dihedral angle (PBEα)
IR806	14 749	2342 (0.29 eV)	0.057	179.60
mTF-IR806	14 430	1061 (0.13 eV)	0.387	177.18
mAn-IR806	14 599	333 (0.04 eV)	0.410	176.82
mPi-IR806	15 105	738 (0.09 eV)	0.463	176.47

nitrogens are indexed as 5 and −5. IR806 has the lowest BLA compared to the other substituted dyes. BLA increases as the electron donation strength for the *meso*-substituent increases. The increase in BLA for the substituted cyanines indicates an increase in the charge-centered resonance structure for the cyanine dye (bis-dipolar configuration).[23]

Our findings were further confirmed by NBO analysis, summarized in Table 2. We note an increased positive charge on the central carbon leading to increased bis-dipolar character. The conjugated backbone slightly departs from planarity, which can be seen as a change in the dihedral angles along the polymethine carbons. This departure from planar structure can be seen in the average dihedral angles along the carbons with indices: 0 to 3, 0 to −3, 1 to 4, and −1 to −4 (Table 2).

To address the observed blue shift in the absorption spectra, as the substituent electron donation strength increases, the vertical excitation energies on the optimized structures were calculated using TDDFT. TDDFT often describes other features of these excitations (such as the shape of the excited PES) reasonably well.[58–60] Typically, vertical excitation energies for the cyanine dyes are poorly described by TDDFT due to the multireference nature for these dyes and their highly delocalized electronic transition, but several functionals have been found to perform better than others for prediction of the vertical excitation energy of the $\pi \rightarrow \pi^*$ excitation of the cyanine dyes, including the PBE functional used in this work.[43,61] The TDDFT vertical excitation energies are calculated at the PBE/6-311+G(3d,p) level and reported in Table 2 along with the associated error in comparison with the experimental absorption maxima. It is worth noting that the error was slightly larger

Fig. 5 Bond length across the conjugated polymethine chain for the optimized ground state structures of the four cyanine dyes. Terminal nitrogens are indexed as −5 and 5.

14090 | *Phys. Chem. Chem. Phys.*, 2017, **19**, 14085–14095

This journal is © the Owner Societies 2017

when employing state-specific PCM solvation rather than the linear response PCM solvation used here. The calculated excitation energies overestimate the experimental value in all cases. Interestingly, the error in the calculated excitation energies for the substituted dyes is smaller than the unsubstituted IR806, which might be attributed to the relative locality of the excitation in the substituted cyanines. The substituted cyanines clearly show an increase in the vertical excitation energies as a function of substituent electron donation strength, as seen experimentally.

In the time-resolved experiments, the molecular response on the positive side of the chirp trace (Fig. 3) and time delay scan, in which the low frequency components of the pulse precede the higher ones (Fig. 4b), can be correlated with the inter-molecular response.[25] In the case of nonpolar response, IR806, the fluorescence signal rises sharply at small chirp and short time delay values. The sudden increase in the signal followed by a gradual decrease has been observed in the chirp scan for indocyanine green (ICG or IR125) when dissolved in ethylene glycol at low temperatures.[25] This was also observed in the time delay scan when ICG was in the pocket of human serum albumin protein.[29] The gradual increase in the fluorescence signal observed for positive chirp is a pattern that was observed with the polar solvated cyanine IR144.[28] The gradual change across the cyanines studied here reflects the difference in their polar solvation response. In the time delay traces for instance, *m*TF-IR806 requires about 120 fs to reach a stable asymptotic fluorescence signal, whereas in the case of *m*Pi-IR806, which has a stronger polar solvation character, it takes about 240 fs to reach the asymptotic signal.

The polar solvation response in substituted cyanine dyes is attributed to the larger change in the dipole moment upon excitation compared to their unsubstituted counterparts.[24,25] This change can be observed in the electron density difference between the excited state TDDFT density and the ground state DFT density as shown in Fig. 6 for IR806 and *m*Pi-IR806 plotted at the same isovalue scale. Upon excitation, the electronic density migrates from the yellow to the blue regions. In the case of IR806, density migration is delocalized over the conjugated system, which is the typical behavior for $\pi \rightarrow \pi^*$ transitions. Charge migration at the chlorine atom can be observed because of the increased density on the polymethine central carbon. *m*Pi-IR806 shows the same delocalized change in the conjugated system electronic density upon excitation. However, density migration from the central carbon to the substituted piperidine is also observed as a small charge transfer from the polymethine backbone to the substituent. This small charge transfer causes the dipole moment to change instantly upon excitation, triggering the polar solvation response for the substituted cyanines. The change in the dipole moment upon excitation is confirmed by our TDDFT/DFT calculations where $\mu_{S_1} - \mu_{S_0}$ for *m*Pi-IR806 was larger (−0.76 Debye) compared to IR806 (−0.54 Debye).

Finally, we focus our attention on the excited-state dynamics of cyanines,[62–67] which is analogous to the dynamics of the protonated Schiff bases and carotenoids.[68–71] Cyanines tend to
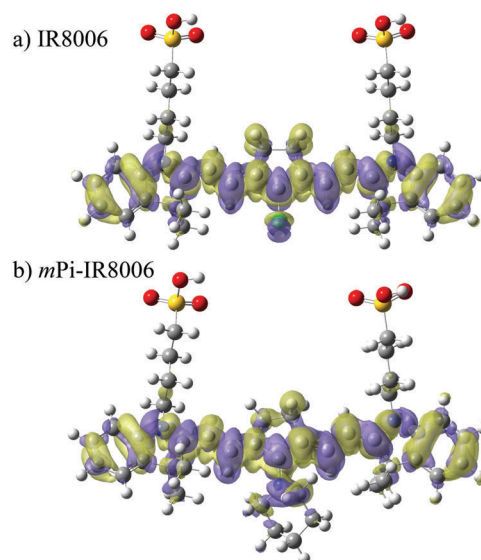

Fig. 6 Electron density difference between the ground and first excited states for (a) IR806 and (b) *m*Pi-IR806. Upon excitation, the electron density migrates from the yellow to the blue regions.

exist in the all-*trans* configuration while in the ground state. Upon photoexcitation, bond lengths across the conjugated system relax and this motion is followed by twisting across one of the bonds in the polyene backbone. In the case of short cyanines, this torsional motion is coupled and barrier-less, leading to a twisted intramolecular charge transfer state (TICT), that is neighboring a conical intersection (CI) with the ground state. For longer cyanine dyes, a significant barrier separates the near-planar geometry from the twisted conformers. Beyond this twisting barrier, the PES descends steeply towards the TICT state and the CI as well. It has been noticed that the barrier to twisting is smallest around the central carbon.[66] Moreover, this energy barrier is lower for the case of *meso*-substituted cyanine dyes compared to their unsubstituted counterparts.[72] In the cyanines considered here, the bonds nearest the central carbon are locked by a cyclopentene ring.

The changes that are observed in the time-resolved experiments (Fig. 3 and 4) when using negative chirp arise from stimulated emission occurring as the excited state wave packet leaves the FC region. Here, we seek to understand the excited state potential energy surface for the different cyanines studied. For this purpose, we modeled the excited state potential energy surfaces of the three cyanines shown in Scheme 2. CN11 represents an unsubstituted cyanine, CN11N has an amine on the central carbon, and CN11NC2 has a dimethilamine substituent. The CASSCF ground state structure was found to be planar only in the case of the unsubstituted CN11, while the substituted dyes were slightly twisted across their polymethine backbones. The amine substituents of both CN11N & CN11NC2 are in a planar sp^2 configuration, which implies electron donation from the substituent and a double bond character between the substituent nitrogen and the cyanine backbone. When following the minimum energy path on the excited state
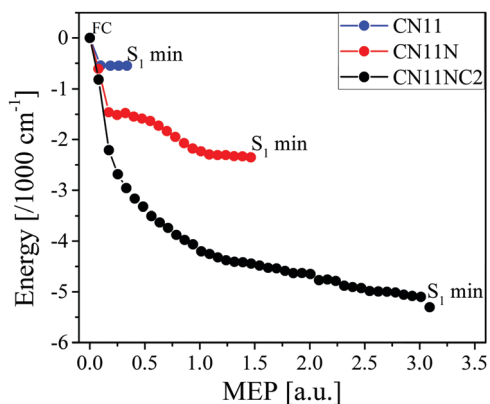
This journal is © the Owner Societies 2017

Phys. Chem. Chem. Phys., 2017, **19**, 14085–14095 | 14091

Fig. 7 The minimum energy path on the first excited state potential from the FC region up to the S$_1$ minima using CASSCF for the three cyanine models.

potential toward equilibrium for each molecule, as shown in Fig. 7, one can clearly see that the largest energy change is associated with CN11NC2, which is the dye with the strongest bis-dipolar character (positive charge in the central position).

The geometric changes associated with excited state energy relaxation are depicted in Fig. 8 for the CASSCF S$_1$ minimum energy paths of the two substituted cyanines; specifically, the dihedrals that describe substituent twisting and pyramidalization are presented. Symmetric changes in $\theta 1$ and $\theta 2$ reflect twisting, while the difference, $\theta 2-\theta 1$, reflects pyramidalization. At the FC geometry, energy relaxation proceeds *via* stretching across the cyanine backbone, similar to the unsubstituted cyanine CN11 and consistent with what is known about long cyanines.[66] However, this mode is coupled with twisting of the substituent while the amine group remains planar. At some twisting point (~ 8 degrees for CN11N, ~ 35 degrees for CN11NC2) the amine substituent undergoes pyramidalization, in which the substituent electron donation begins to diminish.

The final twisting angle was larger for the case of CN11NC2, which explains the largest energy change of that dye during the course of excited state relaxation. It is worth noting that during the substituent twisting and pyramidalization, the cyanine backbone also gradually twists towards a near-planar geometry.

CASPT2 calculations were carried out to validate the above CASSCF potential energy surfaces. It was found that the CASPT2 minimum energy path is somewhat different than that predicted by CASSCF (Fig. S2 in ESI†), but like CASSCF, CASPT2 predicts that the cyanines with the most bis-dipolar character exhibit the largest energy relaxation in the excited state. This can be seen in Fig. 9, which shows two dimensional PESs computed at the CASPT2 level. The two dihedral angles ($\theta 1$ and $\theta 2$) defining the twisting and pyramidalization angles of the substituent were constrained to specific values, and the remaining coordinates were optimized at the CASSCF level of theory. Both the CASSCF energies and the CASPT2 energies are computed at these CASSCF optimized structures. The twisting and pyramidalization angles are reported relative to the substituent position at the FC geometry (the 0,0 angles). The CASSCF potentials show that twisting and pyramidalization are both initially favorable, with a stronger driving force for twisting in CN11NC2. On the other hand, the CASPT2 potentials predict that twisting of the planar substituent by more than 10 degrees is energetically unfavorable, while direct pyramidalization of the untwisted species is energetically downhill. Overall, the relative energy change for the dimethyl amine substituted cyanine (CN11NC2) was larger than for CN11N during the course of energy relaxation on the excited state potential in both the CASSCF and CASPT2 cases. The larger energy relaxation on the excited state potential for the substituted cyanines implies a greater driving force on the wave packet to escape the FC region. Table 3 summarizes the energies at the FC region and the S$_1$ minima using CASSCF and CASPT2//CASSCF for the three cyanines. The CASPT2 S$_1$
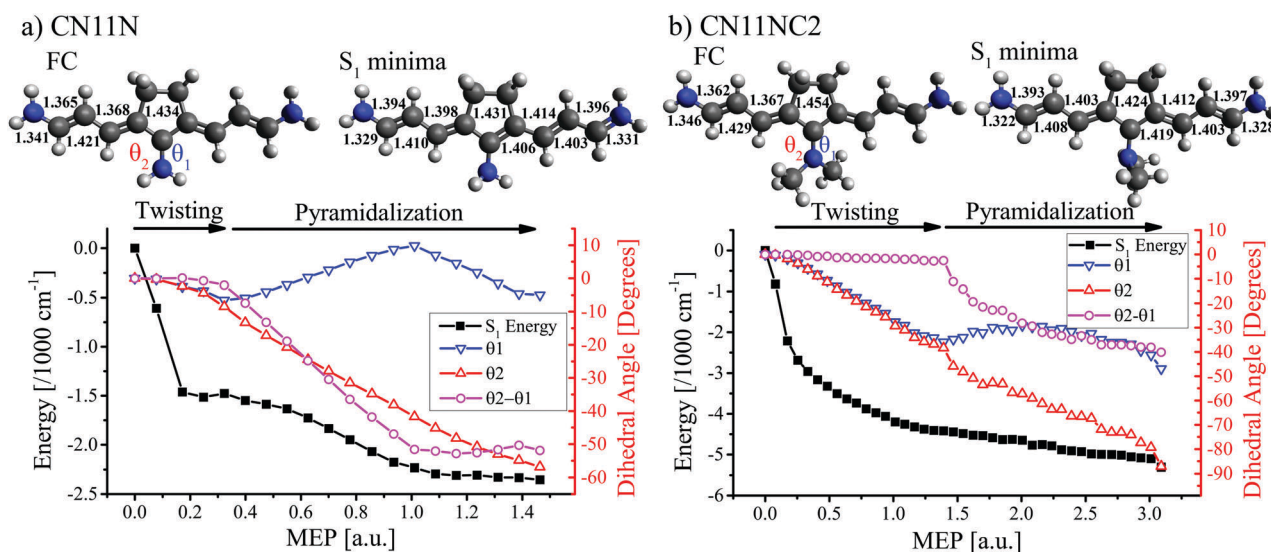

Fig. 8 CASSCF MEP on the S$_1$ potential (filled black) for (a) CN11N and (b) CN11NC2 from the FC region to the emissive S$_1$ minima. Right *y* axis shows the change in the dihedral angles (open colored) compared to the FC geometry.

14092 | *Phys. Chem. Chem. Phys.*, 2017, **19**, 14085–14095

This journal is © the Owner Societies 2017

minima of CN11N and CN11NC2 represent different geometries than the CASSCF S_1 minima, which were estimated from the CASPT2//CASSCF potentials in Fig. 9.

In the time-resolved experiments, differences between the four dyes are greatest for small negative chirp values (Fig. 3), and in the corresponding pump–probe experiments when the high frequency pulse precedes the low frequency pulse (Fig. 4a). IR806 shows a constant fluorescence depletion signal, while the remaining substituted dyes show a relatively greater depletion region at timescales shorter than 200 fs. The relative early time depletion increases according to the following order mTF-IR806 < mAn-IR806 < mPi-IR806, which correlates with their increased bis-dipolar character. Fluorescence depletion is caused by enhanced stimulated emission (Fig. S1 in ESI†),[28] which implies an optimum resonance condition when the excited state wave packet dynamics match the frequencies of the chirped pulse. The fact that the depletion observed at early times is sharper and occurs with higher efficiency (more fluorescence depletion) for the more polar cyanines implies that transient resonance conditions are only met for a short period of time after the wave packet preparation at the FC region. We take this to imply that the wave packet, in the case of

Table 3 Ground and excited state energies at the FC and S_1 minima for the three cyanine models

	CASSCF		CASPT2//CASSCF	
	S_0 (cm^{-1})	S_1 (cm^{-1})	S_0 (cm^{-1})	S_1 (cm^{-1})
CN11 (FC region)	0	17 665	0	19 600
CN11 (S_1 minima)	565	17 100	240	19 035
CN11N (FC region)	0	23 150	0	22 825
CN11N (S_1 minima)	2580	20 810	1325	21 505[a]
CN11NC2 (FC region)	0	24 760	0	23 710
CN11NC2 (S_1 minima)	3645	19 445	2655	21 870[a]

[a] CN11N and CN11NC2 CASPT2//CASSCF minima are different than the CASSCF minima. The minima were obtained from the potentials in Fig. 9.

substituted cyanines, leaves the FC geometry at a faster rate compared to the unsubstituted IR806. Between all the substituted dyes, this rate is the fastest for mPi-IR806, which shows the sharpest and deepest fluorescence depletion. This also implies that the potential energy surface near the FC geometry is steeper. This larger energy relaxation is evident in the calculated excited state potentials of the substituted CN11NC2 and CN11N compared to the unsubstituted CN11, see Fig. 7 and 9.
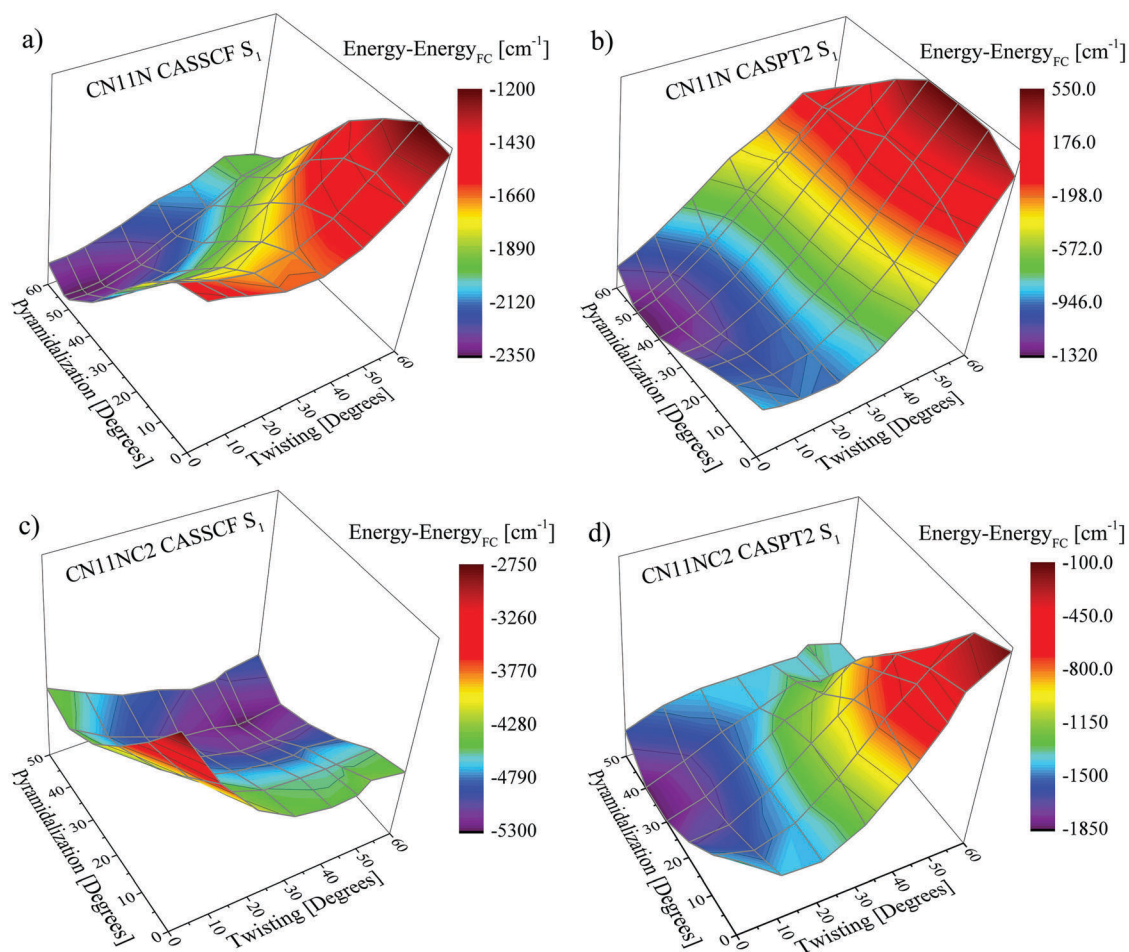
Fig. 9 Optimized S_1 CASSCF and CASPT2//CASSCF potential for (a and b) CN11N and (c and d) CN11NC2 as a function of the two dihedral angles that represent the substituent. The dihedral angles are measured as departure from the FC geometry dihedral angles.

The combination of shaped laser-pulse spectroscopy and *ab initio* theoretical calculations have led to greater insight into the initial excited state dynamics of cyanine molecules. We are also developing a theoretical model based on the density matrix representation for the energy levels in the molecules, in order to model the dynamic evolution of the wave packet as it moves away from the FC region. We hope to report on these efforts in the near future.

Conclusions

The optical properties of cyanine dyes are highly influenced by the electron donation strength of the amine group substituent at the central carbon across the polymethine backbone. These changes affect the initial excited state relaxation dynamics through which multiple intramolecular modes get populated at the FC geometry soon after photoexcitation. Two-color pump-probe and chirped femtosecond pulses were used to measure the relative rates of the excited state energy relaxation across several cyanine dyes with different electronic configurations. The wave packet motion out of the FC region, which is fastest for the cyanine that is substituted with the strongest electron donation group, led to a sharp feature in the fluorescence depletion experiments. Theoretical calculations confirmed the steepness of the excited state potential of substituted cyanines along the twisting and pyramidalization coordinates of the substituent.

Acknowledgements

References

1 P. V. Kumar and M. Maroncelli, *J. Chem. Phys.*, 1995, **103**, 3038–3060.

2 W. P. de Boeij, M. S. Pshenichnikov and D. A. Wiersma, *Annu. Rev. Phys. Chem.*, 1998, **49**, 99–123.

3 M. Glasbeek and H. Zhang, *Chem. Rev.*, 2004, **104**, 1929–1954.

4 A. Rosspeintner, B. Lang and E. Vauthey, *Annu. Rev. Phys. Chem.*, 2013, **64**, 247–271.

5 S. J. Rosenthal, X. Xie, M. Du and G. R. Fleming, *J. Chem. Phys.*, 1991, **95**, 4715–4718.

6 R. Jimenez, G. R. Fleming, P. V. Kumar and M. Maroncelli, *Nature*, 1994, **369**, 471–473.

7 C. C. Jumper, P. C. Arpin, D. B. Turner, S. D. McClure, S. Rafiq, J. C. Dean, J. A. Cina, P. A. Kovac, T. Mirkovic and G. D. Scholes, *J. Phys. Chem. Lett.*, 2016, **7**, 4722–4731.

8 T. Kumpulainen, B. Lang, A. Rosspeintner and E. Vauthey, *Chem. Rev.*, 2016, DOI: 10.1021/acs.chemrev.6b00491.

9 D. M. Jonas, *Annu. Rev. Phys. Chem.*, 2003, **54**, 425–463.

10 P. Nuernberger, S. Ruetzel and T. Brixner, *Angew. Chem., Int. Ed.*, 2015, **54**, 11368–11386.

11 S. Mukamel, *Annu. Rev. Phys. Chem.*, 2000, **51**, 691–729.

12 D. Brinks, R. Hildner, E. M. H. P. van Dijk, F. D. Stefani, J. B. Nieder, J. Hernando and N. F. van Hulst, *Chem. Soc. Rev.*, 2014, **43**, 2476–2491.

13 E. Delaey, F. van Laar, D. De Vos, A. Kamuhabwa, P. Jacobs and P. de Witte, *J. Photochem. Photobiol., B*, 2000, **55**, 27–36.

14 Y. Zhao, G. A. Meek, B. G. Levine and R. R. Lunt, *Adv. Opt. Mater.*, 2014, **2**, 606–611.

15 C. Fang, K. Wang, C. Zeng, C. Chi, W. Shang, J. Ye, Y. Mao, Y. Fan, J. Yang, N. Xiang, N. Zeng, W. Zhu, C. Fang and J. Tian, *Sci. Rep.*, 2016, **6**, 21013.

16 A. Mishra, R. K. Behera, P. K. Behera, B. K. Mishra and G. B. Behera, *Chem. Rev.*, 2000, **100**, 1973–2012.

17 J. L. Bricks, A. D. Kachkovskii, Y. L. Slominskii, A. O. Gerasov and S. V. Popov, *Dyes Pigm.*, 2015, **121**, 238–255.

18 D. K. Das, K. Makhal, S. N. Bandyopadhyay and D. Goswami, *Sci. Rep.*, 2014, **4**, 6097.

19 V. Voiciuk, K. Redeckas, N. A. Derevyanko, A. V. Kulinich, M. Barkauskas, M. Vengris, V. Sirutkaitis and A. A. Ishchenko, *Dyes Pigm.*, 2014, **109**, 120–126.

20 F. Terenziani, O. V. Przhonska, S. Webster, L. A. Padilha, Y. L. Slominsky, I. G. Davydenko, A. O. Gerasov, Y. P. Kovtun, M. P. Shandura, A. D. Kachkovski, D. J. Hagan, E. W. Van Stryland and A. Painelli, *J. Phys. Chem. Lett.*, 2010, **1**, 1800–1804.

21 S. R. Marder, C. B. Gorman, B. G. Tiemann, J. W. Perry, G. Bourhill and K. Mansour, *Science*, 1993, **261**, 186–189.

22 M. Berg, *J. Phys. Chem. A*, 1998, **102**, 17–30.

23 S. Pascal, A. Haefele, C. Monnereau, A. Charaf-Eddin, D. Jacquemin, B. Le Guennic, C. Andraud and O. Maury, *J. Phys. Chem. B*, 2014, **118**, 4038–4047.

24 A. Yu, C. A. Tolbert, D. A. Farrow and D. M. Jonas, *J. Phys. Chem. A*, 2002, **106**, 9407–9419.

25 A. Konar, V. V. Lozovoy and M. Dantus, *J. Phys. Chem. Lett.*, 2014, **5**, 924–928.

26 K. A. Walowicz, I. Pastirk, V. V. Lozovoy and M. Dantus, *J. Phys. Chem. A*, 2002, **106**, 9369–9373.

27 V. V. Lozovoy, I. Pastirk, K. A. Walowicz and M. Dantus, *J. Chem. Phys.*, 2003, **118**, 3187–3196.

28 A. Konar, V. V. Lozovoy and M. Dantus, *J. Phys. Chem. Lett.*, 2012, **3**, 2458–2464.

29 M. Nairat, A. Konar, M. Kaniecki, V. V. Lozovoy and M. Dantus, *Phys. Chem. Chem. Phys.*, 2015, **17**, 5872–5877.

30 A. Konar, V. V. Lozovoy and M. Dantus, *J. Phys. Chem. A*, 2016, **120**, 2002–2008.

31 S.-H. Shim and M. T. Zanni, *Phys. Chem. Chem. Phys.*, 2009, **11**, 748–761.

32 E. Harel, A. F. Fidler and G. S. Engel, *J. Phys. Chem. A*, 2011, **115**, 3787–3796.

33 Y. Rodriguez, F. Frei, A. Cannizzo and T. Feurer, *J. Chem. Phys.*, 2015, **142**, 212451.

14094 | *Phys. Chem. Chem. Phys.*, 2017, **19**, 14085–14095

This journal is © the Owner Societies 2017

34 H. J. B. Marroux and A. J. Orr-Ewing, *J. Phys. Chem. B*, 2016, **120**, 4125–4130.

35 L. Strekowski, M. Lipowska and G. Patonay, *J. Org. Chem.*, 1992, **57**, 4578–4580.

36 Y. Coello, V. V. Lozovoy, T. C. Gunaratne, B. Xu, I. Borukhovich, C.-h. Tseng, T. Weinacht and M. Dantus, *J. Opt. Soc. Am. B*, 2008, **25**, A140–A150.

37 B. Xu, J. M. Gunn, J. M. D. Cruz, V. V. Lozovoy and M. Dantus, *J. Opt. Soc. Am. B*, 2006, **23**, 750–759.

38 G. Rasskazov, V. V. Lozovoy and M. Dantus, *Opt. Express*, 2015, **23**, 23597–23602.

39 J. P. Perdew, M. Ernzerhof and K. Burke, *J. Chem. Phys.*, 1996, **105**, 9982–9985.

40 R. L. Gieseking, M. K. Ravva, V. Coropceanu and J.-L. Brédas, *J. Phys. Chem. C*, 2016, **120**, 9975–9984.

41 E. D. Glendening, J. K. Badenhoop, A. E. Reed, J. E. Carpenter, J. A. Bohmann, C. M. Morales, C. R. Landis and F. Weinhold, *NBO 6.0*, Theoretical Chemistry Institute, University of Wisconsin, Madison, 2013.

42 J. P. Perdew, K. Burke and M. Ernzerhof, *Phys. Rev. Lett.*, 1996, **77**, 3865–3868.

43 D. Jacquemin, Y. Zhao, R. Valero, C. Adamo, I. Ciofini and D. G. Truhlar, *J. Chem. Theory Comput.*, 2012, **8**, 1255–1259.

44 S. Karaca and N. Elmacı, *Comput. Theor. Chem.*, 2011, **964**, 160–168.

45 E. Cancès, B. Mennucci and J. Tomasi, *J. Chem. Phys.*, 1997, **107**, 3032–3041.

46 G. Ghigo, B. O. Roos and P.-Å. Malmqvist, *Chem. Phys. Lett.*, 2004, **396**, 142–149.

47 M. J. Frisch, G. W. Trucks, H. B. Schlegel, G. E. Scuseria, M. A. Robb, J. R. Cheeseman, G. Scalmani, V. Barone, B. Mennucci, G. A. Petersson, H. Nakatsuji, M. Caricato, X. Li, H. P. Hratchian, A. F. Izmaylov, J. Bloino, G. Zheng, J. L. Sonnenberg, M. Hada, M. Ehara, K. Toyota, R. Fukuda, J. Hasegawa, M. Ishida, T. Nakajima, Y. Honda, O. Kitao, H. Nakai, T. Vreven, J. A. Montgomery Jr., J. E. Peralta, F. Ogliaro, M. J. Bearpark, J. Heyd, E. N. Brothers, K. N. Kudin, V. N. Staroverov, R. Kobayashi, J. Normand, K. Raghavachari, A. P. Rendell, J. C. Burant, S. S. Iyengar, J. Tomasi, M. Cossi, N. Rega, N. J. Millam, M. Klene, J. E. Knox, J. B. Cross, V. Bakken, C. Adamo, J. Jaramillo, R. Gomperts, R. E. Stratmann, O. Yazyev, A. J. Austin, R. Cammi, C. Pomelli, J. W. Ochterski, R. L. Martin, K. Morokuma, V. G. Zakrzewski, G. A. Voth, P. Salvador, J. J. Dannenberg, S. Dapprich, A. D. Daniels, Ö. Farkas, J. B. Foresman, J. V. Ortiz, J. Cioslowski and D. J. Fox, *Gaussian 09, Revision D.01*, Gaussian, Inc., Wallingford, CT, USA, 2009.

48 H.-J. Werner, P. J. Knowles, G. Knizia, F. R. Manby and M. Schütz, *Wiley Interdiscip. Rev.: Comput. Mol. Sci.*, 2012, **2**, 242–253.

49 H.-J. Werner, P. J. Knowles, G. Knizia, F. R. Manby, M. Schütz, P. Celani, W. Györffy, D. Kats, T. Korona, R. Lindh, A. Mitrushenkov, G. Rauhut, K. R. Shamasundar, T. B. Adler, R. D. Amos, A. Bernhardsson, A. Berning, D. L. Cooper, M. J. O. Deegan, A. J. Dobbyn, F. Eckert, E. Goll, C. Hampel, A. Hesselmann, G. Hetzer, T. Hrenar, G. Jansen, C. Köppl, Y. Liu, A. W. Lloyd, R. A. Mata, A. J. May,

S. J. McNicholas, W. Meyer, M. E. Mura, A. Nicklaß, D. P. O'Neill, P. Palmieri, D. Peng, K. Pflüger, R. Pitzer, M. Reiher, T. Shiozaki, H. Stoll, A. J. Stone, R. Tarroni, T. Thorsteinsson and M. Wang, *MOLPRO, Version 2012.1, a Package of Ab Initio Programs*, see http://www.molpro.net.

50 H.-J. Werner and P. J. Knowles, *J. Chem. Phys.*, 1985, **82**, 5053–5063.

51 T. Busch, A. D. Esposti and H.-J. Werner, *J. Chem. Phys.*, 1991, **94**, 6708–6715.

52 P. Celani and H.-J. Werner, *J. Chem. Phys.*, 2000, **112**, 5546–5557.

53 M. Nairat, A. Konar, V. V. Lozovoy, W. F. Beck, G. J. Blanchard and M. Dantus, *J. Phys. Chem. A*, 2016, **120**, 1876–1885.

54 C. A. Guarin, J. P. Villabona-Monsalve, R. López-Arteaga and J. Peon, *J. Phys. Chem. B*, 2013, **117**, 7352–7362.

55 G. Cerullo, C. J. Bardeen, Q. Wang and C. V. Shank, *Chem. Phys. Lett.*, 1996, **262**, 362–368.

56 S. R. Marder, C. B. Gorman, F. Meyers, J. W. Perry, G. Bourhill, J.-L. Brédas and B. M. Pierce, *Science*, 1994, **265**, 632–635.

57 S. Ohira, J. M. Hales, K. J. Thorley, H. L. Anderson, J. W. Perry and J.-L. Brédas, *J. Am. Chem. Soc.*, 2009, **131**, 6099–6101.

58 D. Jacquemin, E. A. Perpète, I. Ciofini, C. Adamo, R. Valero, Y. Zhao and D. G. Truhlar, *J. Chem. Theory Comput.*, 2010, **6**, 2071–2085.

59 B. Le Guennic and D. Jacquemin, *Acc. Chem. Res.*, 2015, **48**, 530–537.

60 H. Zhekova, M. Krykunov, J. Autschbach and T. Ziegler, *J. Chem. Theory Comput.*, 2014, **10**, 3299–3307.

61 R. Send, O. Valsson and C. Filippi, *J. Chem. Theory Comput.*, 2011, **7**, 444–455.

62 Z. Wei, T. Nakamura, S. Takeuchi and T. Tahara, *J. Am. Chem. Soc.*, 2011, **133**, 8205–8210.

63 M. M. Bishop, J. D. Roscioli, S. Ghosh, J. J. Mueller, N. C. Shepherd and W. F. Beck, *J. Phys. Chem. B*, 2015, **119**, 6905–6915.

64 A. Weigel, M. Pfaffe, M. Sajadi, R. Mahrwald, R. Improta, V. Barone, D. Polli, G. Cerullo, N. P. Ernsting and F. Santoro, *Phys. Chem. Chem. Phys.*, 2012, **14**, 13350–13364.

65 B. Dietzek, T. Pascher and A. Yartsev, *J. Phys. Chem. B*, 2007, **111**, 6034–6041.

66 A. Sanchez-Galvez, P. Hunt, M. A. Robb, M. Olivucci, T. Vreven and H. B. Schlegel, *J. Am. Chem. Soc.*, 2000, **122**, 2911–2924.

67 P. A. Hunt and M. A. Robb, *J. Am. Chem. Soc.*, 2005, **127**, 5720–5726.

68 L. A. Peteanu, R. W. Schoenlein, Q. Wang, R. A. Mathies and C. V. Shank, *Proc. Natl. Acad. Sci. U. S. A.*, 1993, **90**, 11762–11766.

69 I. Rivalta, A. Nenov and M. Garavelli, *Phys. Chem. Chem. Phys.*, 2014, **16**, 16865–16879.

70 M. Garavelli, T. Vreven, P. Celani, F. Bernardi, M. A. Robb and M. Olivucci, *J. Am. Chem. Soc.*, 1998, **120**, 1285–1288.

71 S. Ghosh, J. D. Roscioli, M. M. Bishop, J. K. Gurchiek, A. M. LaFountain, H. A. Frank and W. F. Beck, *J. Phys. Chem. Lett.*, 2016, **7**, 3621–3626.

72 J. Cao, C. Hu, W. Sun, Q. Xu, J. Fan, F. Song, S. Sun and X. Peng, *RSC Adv.*, 2014, **4**, 13385–13394.